Editors' Suggestion

Resistive and ballistic phonon transport in β-Ga_2O_3

R. Ahrling,[1] R. Mitdank,[1] A. Popp,[2] J. Rehm,[2] A. Akhtar,[2] Z. Galazka,[2] and S. F. Fischer[1,3,*]

[1]*Novel Materials Group, Humboldt-Universität zu Berlin, Newtonstraße 15, 12489 Berlin, Germany*

[2]*Leibniz-Institut für Kristallzüchtung, Max-Born-Straße 2, 12489 Berlin, Germany*

[3]*Center for the Science of Materials, Humboldt-Universität zu Berlin, Zum Großen Windkanal 2, 12489 Berlin, Germany*

(Received 5 April 2024; accepted 26 July 2024; published 14 August 2024)

The anisotropic thermal conductivity and the phonon mean free path (mfp) in monoclinic β-Ga_2O_3 single crystals and homoepitaxial (HE) films of several microns were determined using the 3ω method in the temperature range from 10 to 300 K. The measured effective thermal conductivity of both single-crystal and HE films are on the order of 20 W/(mK) at room temperature; <30 K, it increases with a maximum of 1000 to 2000 W/(mK) and decreases with T^3 < 25 K. Analysis of the phonon mfp shows the dominance of phonon-phonon-Umklapp scattering >80 K, below which the influence of point-defect scattering is observed. Below 30 K, the phonon mfp increases until it is limited by the total β-Ga_2O_3 sample size. A crossover from resistive to ballistic phonon transport is observed <20 K, and boundary effects of the total sample size become dominant. This reveals that the HE film-substrate interface is highly phonon transparent. The resistive and ballistic phonon transport regimes in β-Ga_2O_3 are discussed corresponding to the models of Callaway and Majumdar, respectively.

DOI: 10.1103/PhysRevB.110.085302

I. INTRODUCTION

Gallium oxide (Ga_2O_3) is a transparent ultrawide band gap (4.7–4.9 eV) [1–3] semiconductor of topical research interest for deep-ultraviolet devices, gas sensors, and high-power electronic applications [4–12] with a predicted breakthrough electric field of $E_b = 8$ MV/cm [8], exceeding that of currently used materials in high-power electronics ($E_b \approx 2.5$ MV/cm for SiC and $E_b \approx 3.3$ MV/cm for GaN) [13]. The most stable form is the polymorph β-Ga_2O_3.

However, a major challenge in electronic device design is heat dissipation. It was shown that the room-temperature thermal conductivity of bulk β-Ga_2O_3 [14,15] is more than one order of magnitude lower than those of bulk GaN and SiC [16]. An anisotropic thermal conductivity of single crystalline β-Ga_2O_3 due to the monoclinic crystal structure has been reported at room temperature: The highest value is determined along the [010] direction of 27 W/(mK) via time domain thermoreflection [14], 22 W/(mK) via laser-flash [15], and 29 W/(mK) with 2ω and 3ω measurements [17,18]. Below room temperature, thermal conductivities of 200–300 W/(mK) at 80 K [14] and 190 W/(mK) at 60 K [17] have been reported. The low-temperature regime (<60 K) which is relevant for point-defect and boundary-limited heat transport remains an open issue.

Here, we investigate the thermal transport properties in the full temperature regime between 10 and 300 K of single-crystalline substrates and homoepitaxially (HE) grown thin films as typically used in high-power electronic devices. We identify the scattering mechanisms and the crossover from resistive to ballistic phonon transport.

In general, *heteroepitaxially* grown β-Ga_2O_3 films exhibit a reduced room-temperature thermal conductivity compared with bulk. Reductions of 50 and 35% for a 2 μm film [19] and 400-nm-thin β-Ga_2O_3 exfoliated films on quartz glass [20], respectively, have been observed. From this, it follows that, to maintain the maximal thermal conductivities, single crystals and HE grown films of high crystalline quality and purity are required because defects lower the thermal conductivity [17,18,21]. However, thermal transport through epitaxial interfaces realized by HE grown β-Ga_2O_3 films on a β-Ga_2O_3 single-crystal substrate has not yet been reported.

While intrinsic phonon scattering consisting of Umklapp and point-defect scattering is known to dominate the thermal transport for temperatures >100 K [17,18], a crossover from resistive to ballistic phonon transport at lower temperatures may occur in high-quality β-Ga_2O_3 single crystals and in HE grown epilayers on single-crystalline substrates. In the ballistic regime, phonons do not undergo resistive scattering, and the two sample surfaces are each in thermal equilibrium with the attached heat bath emitting and absorbing phonons [22]. This is described as phonon-radiative transport (PRT) [23,24]. For this case, the sound velocity is the only relevant material parameter, while the specific heat of the crystal no longer plays a role. The properties of the sample surfaces fully determine the heat transport [24]. The transport regimes are expressed by different relevant mean free paths (mfps), as introduced below. At higher temperatures, the phonon transport is resistive. In the Callaway model [25] a mfp Λ_C is defined, calculated with Matthiessens rule as

$$\frac{1}{\Lambda_C} = \frac{1}{\Lambda_U} + \frac{1}{\Lambda_{PD}} + \frac{1}{\Lambda_B}, \tag{1}$$

where Λ_U depicts the mfp by sole contribution of Umklapp scattering, Λ_{PD} depicts the mfp by a sole contribution of

*Contact author: sfischer@physik.hu-berlin.de

point-defect scattering, and Λ_B is the mfp attributed to the contribution of boundary scattering.

The intrinsic mfp Λ is defined for a theoretically infinite crystal without the influence of any boundary effects. For Λ, only Umklapp and point-defect scattering are considered $\frac{1}{\Lambda} = \frac{1}{\Lambda_U} + \frac{1}{\Lambda_{PD}}$. If the intrinsic mfp Λ compares with the total sample thickness d, the heat transport from heater to the backside of the crystal is ballistic. A model describing the transition from resistive to ballistic transport well is given by Majumdar [24]. Here, the resistive scattering model from Callaway [25] merges with the ballistic transport model from Casimir [22]. An *effective* mfp:

$$\Lambda_{\text{eff}} = \frac{\Lambda}{1 + \frac{4}{3} \cdot \frac{\Lambda}{d}}, \tag{2}$$

is introduced by Majumdar [24].

The PRT as described in the model of Majumdar is formally exchanged by an adequate boundary scattering model. For $\Lambda = d$, the effective mfp then becomes $\Lambda_{\text{eff}} = \frac{3}{7}d$. In the case of $\Lambda \gg d$, Λ_{eff} approximates instead to $\frac{3}{4}d$, which is often named the Casimir limit [22].

For both the resistive as well as the ballistic transport regime, T^3 dependence of the thermal conductivity is expected [23,24], however, for different physical reasons: The temperature dependence of thermal conductivity in the resistive regime is governed by that of the specific heat as $C \propto T^3$. Instead, in the regime of ballistic phonon transport, a thermal equilibrium of emission and absorption of phonons between heater and substrate is established, and the temperature dependence of the thermal conductivity is proportional to T^3 due to the radiation laws as first described by Casimir for PRT [22]. This is included in the model of Majumdar [24], in which only the sound velocity remains as a relevant material parameter. Therefore, the T^3 relation of the thermal conductivity at low temperature is a prerequisite but not sufficient for the identification of ballistic phonon transport. However, if additionally the determined mfp compares with the sample thickness, ballistic transport takes place.

Therefore, to tackle the problem of heat dissipation in β-Ga_2O_3 devices, fundamental research about the heat flow through β-Ga_2O_3 interfaces is necessary for a wide range of temperatures [16]. Recently, we have shown that, for sufficiently high-quality material, the heat transport is dominated by Umklapp scattering for temperatures >100 K [17,18]. From the considerations as given above, the expectation is that, for lower temperatures, heat can be transported ballistically through the crystal, and the properties of the sample surfaces determine the energy transport depending on the sample thickness [22]. For this reason, we expand the previously reported lower temperature limit for thermal conductivity measurements on β-Ga_2O_3 from 60 K [17] to 10 K to observe ballistic effects and draw conclusions about the interactions between phonons and interfaces. The thermal conductivity and phonon mfp in β-Ga_2O_3 single crystals and HE grown β-Ga_2O_3 thin films on β-Ga_2O_3 single crystals are determined from 3ω measurements between 10 and 300 K. Based on these data, the resistive and ballistic phonon transport regimes are identified.

II. EXPERIMENT

Electrically insulating single-crystalline substrates were prepared from Czochralski grown Mg-compensation doped crystals as described in detail elsewhere [26–29]. They were oriented, cut into $10 \times 10\,\text{mm}^2$ bars in the cross-section, and cleaved parallel to the (100) plane.

For the growth of HE films, the (100)-oriented substrates have been polished with a 4 ° off cut prepared toward the [00-[1]] direction. This provides vicinal surfaces to allow for a layer growth in smooth step-flow growth mode. In the next step, HE films of 2 and 3 μm β-Ga_2O_3 have been grown on the substrates via metalorganic vapor-phase epitaxy (MOVPE) [30,31]. These HE layers are denoted in the following as SCB + 2 μm HE and SCB + 3 μm HE, while the single-crystalline bulk sample is denoted as SCB in this paper.

X-ray diffraction (XRD) measurements show that the highest crystal lattice quality is achieved for the SCB sample with a full width at half maximum (FWHM) of 29 arcsec, as shown in Fig. 1(a). This is in good agreement with previously reported MOVPE samples of high growth quality [31]. The structural quality of the HE film samples has been measured to either be of similar quality (FWHM = 31 arcsec for the SCB + 2 μm HE sample) or only slightly decreased compared with the bulk (FWHM = 45 arcsec for the SCB + 3 μm HE sample). The morphology of the surface of the grown HE layer has been measured by atomic force microscopy (AFM). A representative picture is shown in Fig. 1(b) for a 3-μm-thick HE layer. In this case, the desired step-flow growth mode has not been stabilized up to 3 μm. As a result, a superimposing of several steps occurred, leading to the step-bunching effect shown here.

The roughness of the polished SCB sample surfaces has been determined by AFM to be on the order of 1 nm, while the roughness of the unpolished backside is on the order of 5 μm. Transmission electron microscopy (TEM) imaging (see, e.g., Fig. S4 in the Supplemental Material [32]), and comparison with other samples revealed no visible accumulation of defects at the interface between the SCB substrate and HE layer. For the full details on growth process and crystallographic analysis, see Refs. [26–30].

To determine the thermal conductivity by 3ω measurements, metal line structures [shown in Fig. 1(c)] were fabricated on top of each of the β-Ga_2O_3 sample surfaces using photolithography with positive resist AZ ECI 3027, magnetron sputtering of Ti/Au (5 nm/50 nm) and subsequent lift-off in an ultrasonic bath of DMSO. In this paper, all metal lines were bonded with Au wire to form Schottky contacts. The formation of Schottky contacts and the high resistivity of all β-Ga_2O_3 samples with respect to the low metallic resistance of the heater lines prevent electrical currents in the full temperature range from 10 to 300 K. As detailed in previous reports, the applied ac currents flow only in the metallic line structures [14,15]. In accordance with the Bloch-Grüneisen law for the temperature dependence of metals (c.f. Ref. [14]), the temperature coefficient of the metal line heater is almost constant with only a slight increase with decreasing bath temperature down to 30 K. Below, it decreases significantly (see Fig. S1 in the Supplemental Material [32]), and the temperature dependence of the resistance of the metallic heater line deviates from the linear temperature dependence.

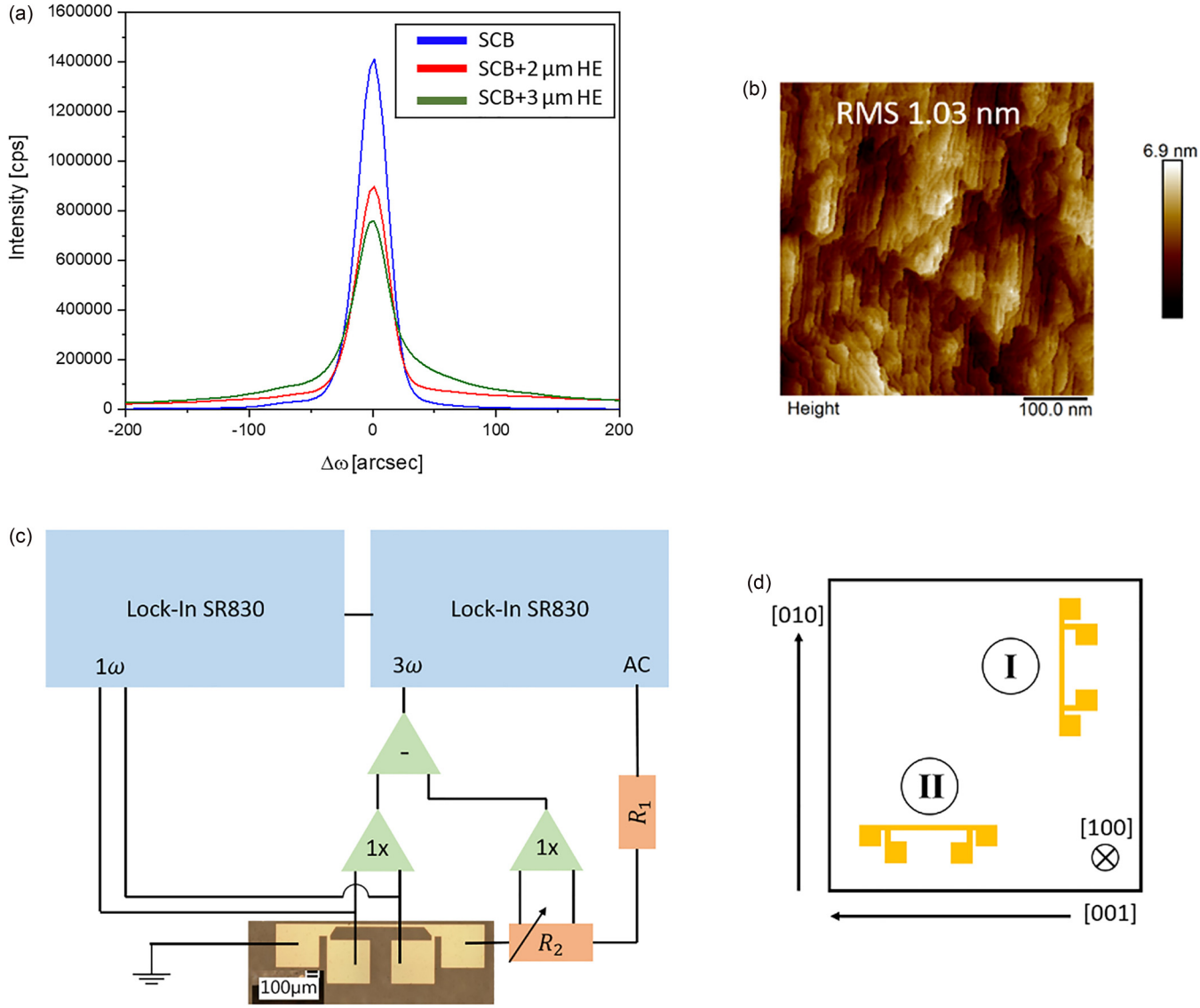

FIG. 1. Overview of the material quality, measurement setup, and sample geometry. (a) X-ray diffraction (XRD) measurement of the single-crystalline bulk (SCB) sample [full width at half maximum (FWHM) = 29 arcsec], SCB + 2 µm HE sample (FWHM = 31 arcsec) and SCB + 3 µm HE sample (FWHM = 45 arcsec). (b) atomic force microscopy (AFM) image of the sample surface morphology after homoepitaxial growth of a 3 µm film. (c) Measurement setup for the 3ω-voltage measurements. (d) Schematic of the measurement structures on the sample, measuring in two different geometries: I denotes measurements of the heat flow in the combined [100]/[001] direction; II denotes measurements of the heat flow in the combined [100]/[010] direction.

Therefore, it is of utmost importance that, for low bath temperatures T, the temperature oscillations ΔT imposed on the metal lines remain small. In this case, a linear approximation is still possible, and the dominating linear component which is responsible for the 3ω-voltage signal (as required for the thermal conductivity measurement and discussed below) is selected by lock-in measurement technique. At a bath temperature of 10 K, a temperature change of $\Delta T < 0.3$ K results in a ratio $\Delta T/T$ of <3%. For the whole temperature range, we have ensured that the condition $\Delta T/T << 1$ is fulfilled.

In this paper, the 3ω method [33,34] was used to determine the thermal conductivity of the SCB, SCB + 2 µm HE, and SCB + 3 µm HE samples. Driving an AC current I with angular frequency $\omega = 2\pi f$ through the outer contacts of the metal heater lines placed on each of the samples causes a temperature oscillation ΔT due to Joule heating. Since the heating power is $P = RI^2$, with R as resistance of the metal line, the temperature oscillation will be $\Delta T \propto \cos(2\omega t)$. Due to the temperature dependence of the metal line resistance of $R = R_0(1 + \alpha \Delta T)$, this resistance will also oscillate as $R \propto \cos(2\omega t)$. The temperature coefficient α and the resistance R_0 are functions of the bath temperature T_0, as seen in Fig. S1 in the Supplemental Material [32]. Therefore, the voltage between the inner metal line contacts $U = RI$ has two components $U_{1\omega} \propto \cos(\omega t)$ and $U_{3\omega} \propto \cos(3\omega t)$. The 3$\omega$-voltage signal contains information about the temperature increase ΔT and thermal conductivity λ of the sample. Assuming $\alpha \Delta T \ll 2$ (this condition is proven to hold true over the entire

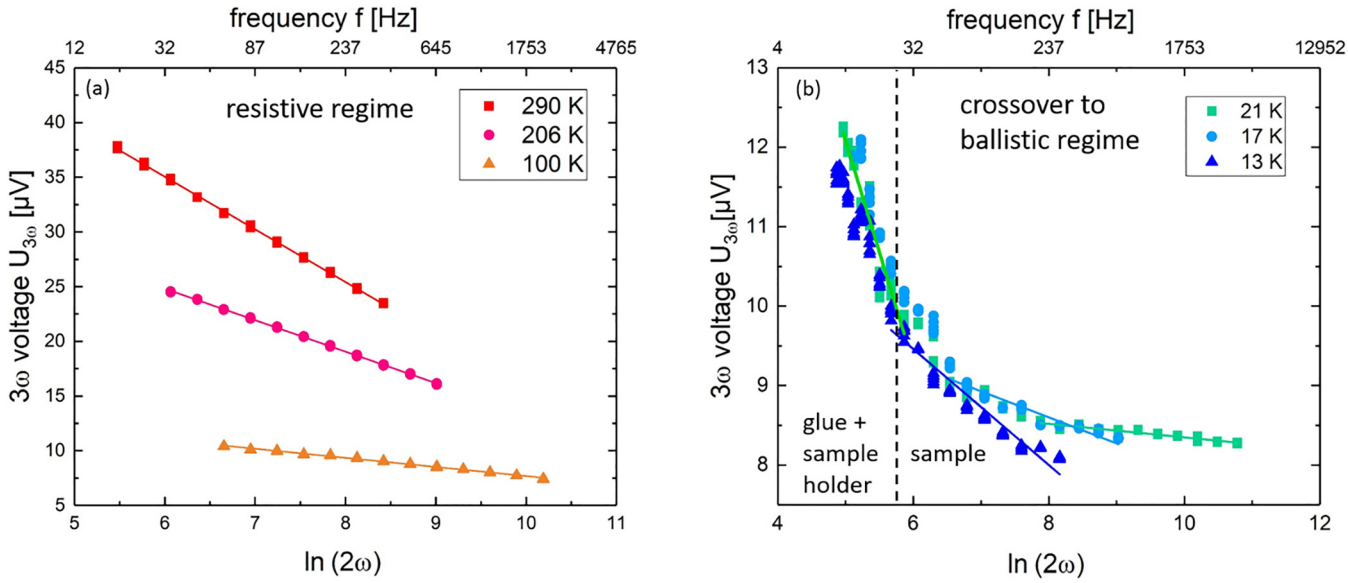

FIG. 2. Measured 3ω voltage as a function of the logarithmic frequency. The data are taken from the SCB+3 μm HE sample in the [100]/[010] configuration (II). (a) Resistive thermal transport regime (Umklapp) for high temperatures (290–100 K). (b) Crossover to the ballistic thermal transport regime at low temperatures (21–13 K). In both cases, the linear dependence $U_{3\omega} \propto \ln(2\omega)$ can clearly be seen. Different frequency bands used for evaluation stem from a temperature-dependent thermal penetration depth.

temperature range, see Fig. S1 in the Supplemental Material [32]), the temperature oscillation can be experimentally determined to be

$$\Delta T = \frac{2U_{3\omega}}{\alpha U_{1\omega}}. \tag{3}$$

It can be shown that

$$\Delta T = \frac{P}{l\pi\lambda}\left(\frac{1}{2}\ln\frac{D}{b^2} + \ln 2 - 0,5772 - \frac{i\pi}{4} - \frac{1}{2}\ln 2\omega\right), \tag{4}$$

where D is the thermal diffusivity of the sample and b the heater line width [33,35].

Combining these equations, the thermal conductivity can be extracted from the slope of $U_{3\omega}$ vs $\ln 2\omega$, and it is $\lambda = \frac{\alpha U_{1\omega}^3}{4\pi l R} \cdot \frac{\Delta \ln 2\omega}{\Delta U_{3\omega}}$. The heating voltage is provided by the output of a SR 830 lock-in amplifier. With two such lock-in amplifiers, the 1ω- and 3ω-voltage signals are measured simultaneously. The heater line is put in series with a potentiometer to equilibrate and remove the 1ω-voltage signal by using a differential amplifier. This is done to detect the smaller 3ω signal. A schematic of the measurement setup is shown in Fig. 1(c).

Temperature-dependent measurements were performed in a KONTI IT flow cryostat. To minimize influences of thermal convection of the surrounding He atmosphere, the sample chamber was held under vacuum. The influence of thermal radiation can be neglected in the temperature range examined in this paper [36].

Here, 3ω-voltage measurements were performed on each of the three samples (SCB, SCB + 2 μm HE, and SCB + 3 μm HE) with two perpendicular heater orientations (I and II), see Fig. 1(c). Due to the monoclinic β-Ga_2O_3 crystal structure, the 3ω-voltage measurement detects the mean thermal conductivity of the two directions—in-plane and cross-plane—perpendicular to the heater direction. In this paper, we determine the heat flow in measurement configurations (I) of the combined [100]/[001] direction and (II) combined [100]/[010] direction, see Fig. 1(d).

III. RESULTS

Representative 3ω-voltage measurements are shown in Fig. 2. The linear dependence of 3ω voltage and logarithmic frequency holds up for all temperatures in their corresponding frequency bands. These measurements confirm the linear relation between $U_{3\omega}$ and $\ln 2\omega$. The gradient $\Delta U_{3\omega}/\Delta \ln 2\omega$ decreases for lower temperatures, which indicates a rise in thermal conductivity, see Fig. 2(a). Below 30 K, this gradient increases, indicating a decline in thermal conductivity, see Fig. 2(b). These temperature dependencies will be discussed in the following. For low temperatures, as depicted in Fig. 2(b), the low-frequency data show a different slope which originates from the sample holder, yielding a similar value for all shown temperatures. Here, the thermal penetration depth exceeds the total β-Ga_2O_3 sample thickness.

For room temperature (293 K), the measured effective thermal conductivities are determined as $\lambda_{[100]/[010]} = (20 \pm 2)$ W/(mK), with good agreement between all measured samples and as $\lambda_{[100]/[001]} = (19 \pm 2)$ W/(mK). Overall, this confirms previous reports [14,16,17,37], in which the thermal conductivity is highest in the [010] direction under the assumption that the thermal conductivity in the [100] is the lowest.

However, the SCB + 3 μm HE sample shows a reduced value of $\lambda_{[100]/[001]} = (14 \pm 1)$ W/(mK). This reduced value for $\lambda_{[100]/[001]}$ in the 3 μm sample may occur due to growth defects in the epitaxial layer induced by the step-bunched growth morphology [see Fig. 1(b)]. These defects tend to elongate in the (001) planes, which is expected since they are macro steps resulting from destabilized step flow growth. The

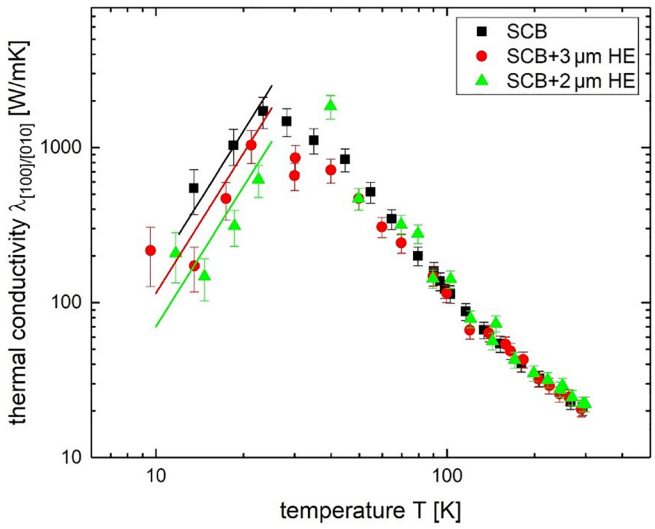

FIG. 3. Measured thermal conductivity in the [100]/[010] configuration II as a function of the temperature. Data of three samples are shown: single-crystalline bulk (SCB; black squares), SCB + 3 µm HE (red circles), and SCB + 2 µm HE (green triangles). The lines act as a guide for the eye.

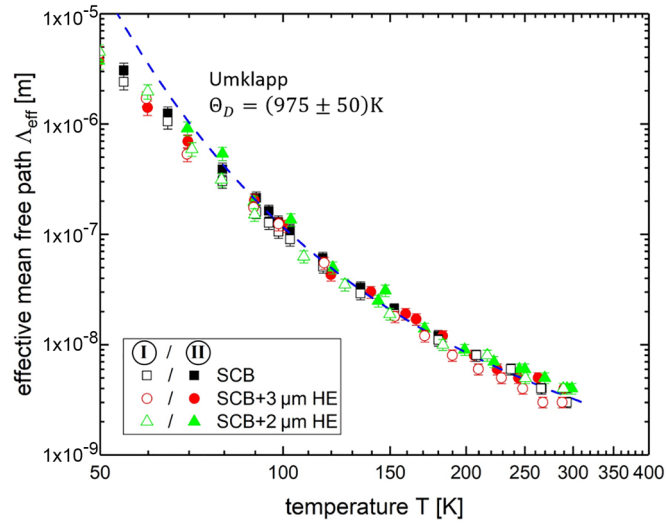

FIG. 4. Effective phonon mean free path (mfp) as a function of temperature for the single-crystalline with and without homoepitaxial layer β-Ga_2O_3 samples. Both measurement configurations I and II are shown. The effective phonon mfps show no anisotropy with respect to crystal orientation. The model of Umklapp scattering (blue dashed line) was used to describe the temperature regime >80 K. Deviations from this model begin only <80 K.

step-bunched surface morphology could explain a reduction in heat transport dependent on the crystal direction [38]. The deviation occurs only for temperatures >200 K. Here, the phonon mfp is much smaller than the thickness of the epitaxial layer of 3 µm, and the thermal penetration depth is of comparable order of magnitude (see Fig. S7 in the Supplemental Material [32]). Therefore, the 3ω-voltage measurement is sensitive to the defects in the layer in this temperature regime.

To compare the determined values of the thermal conductivity with those reported previously, it must be considered that a 3ω measurement on an anisotropic crystal will always yield the mean value of both directions perpendicular to the heater line direction $\lambda_{xy} = \frac{\lambda_x + \lambda_y}{2}$. Values calculated from the literature in this way are compared with those of this paper in Table S2 in the Supplemental Material [32]. For configuration II, the measurements are well in accordance with previously reported values. For configuration I (see Fig. S5 in the Supplemental Material [32]), the measurements exceed our previously measured values [14,16,17,18] by ∼10%, while the theoretically predicted value [37] is in agreement. This indicates a higher material quality in this paper, as explained below.

As expected, the thermal conductivity increases with decreasing temperature, see Fig. 3. Below 80–90 K, a change in the slope of the double logarithmic plot can be observed, indicating a change in the dominant phonon scattering mechanism. Here, the anisotropy between both measurement configurations also diminishes. Maximum thermal conductivity is reached for all samples ∼25–30 K with values of 1000–3000 W/(mK).

For temperatures <25 K, the thermal conductivity decreases with decreasing temperature. In this regime, T^3 dependence of the thermal conductivity is expected, as detailed in the introduction.

IV. DISCUSSION

From the measured thermal conductivities, the effective phonon mfp can be calculated as

$$\Lambda_{\text{eff}} = \frac{3\lambda}{v_S c_p \rho}. \tag{5}$$

Since the measured thermal conductivities are mean values of two directions, the corresponding mean values of the sound velocities (Guo *et al.* [16]) are applied.

The overall temperature dependence of the phonon mfp can be seen in Figs. 4 and 5. It increases with a decrease in temperature. Below 25–30 K, the mfp begins to flatten out, reaching a plateau at a value of $\frac{3}{7}d = 214\,\mu$m, indicating a crossover from resistive to ballistic phonon transport.

A fit for the mfp over the entire temperature range was applied by a combination of phonon-phonon-Umklapp scattering and point-defect scattering as given by the Callaway model [25] for intrinsic scattering:

$$\frac{1}{\Lambda} = \frac{1}{\Lambda_U} + \frac{1}{\Lambda_{PD}}.$$

The Umklapp scattering is given by

$$\Lambda_U \propto \left[\exp\left(\frac{\Theta_D}{2T}\right) - 1\right]. \tag{6}$$

Between 30 and 80 K, point-defect scattering plays a relevant role, and it is modeled as

$$\Lambda_{\text{PD}} \propto T^{-4}, \tag{7}$$

analogous to Rayleigh scattering.

Below 30 K, scattering at the surface boundaries becomes dominant, and if the effective mfp Λ compares with the overall sample thickness d, a constant mfp of $\Lambda_{\text{B}} = \frac{3}{7}d$ according

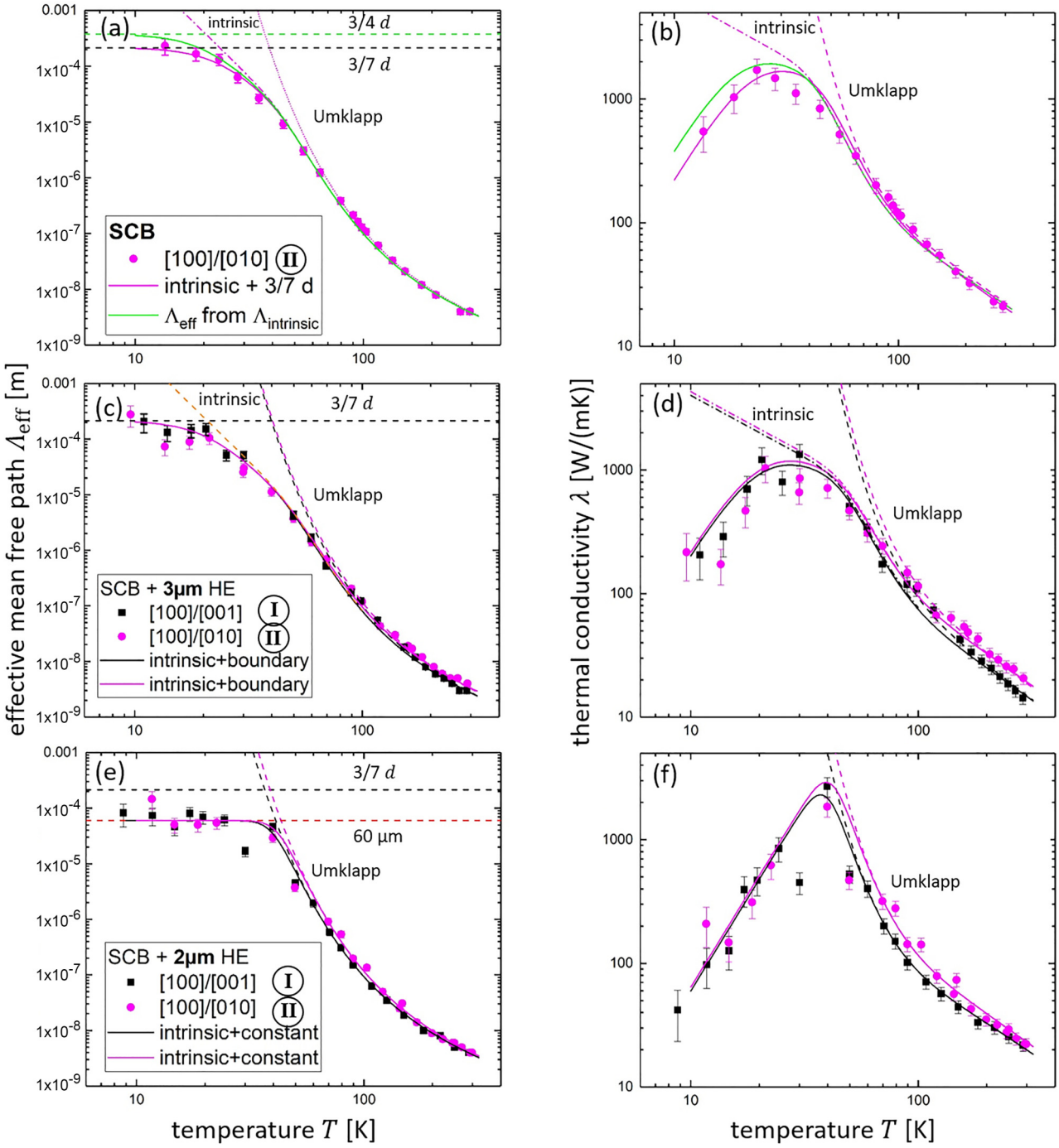

FIG. 5. Detailed analysis. Left column: (a), (c), and (e) Effective mean free paths (mfps) calculated from measured thermal conductivities fitted after the models of Callaway (high T) and Majumdar (low T). Right column: (b), (d), and (f) Fits from the curves in the left column applied to the measured thermal conductivities. (a) Effective phonon mfp, calculated from the measured thermal conductivity, as a function of temperature on the single-crystalline bulk (SCB) sample (configuration II). A model including Umklapp scattering, point defect scattering, and a constant mfp of $\frac{3}{7}d = 214\,\mu$m fits the effective mfp data well. (b) Thermal conductivity as a function of temperature on the SCB sample. The data have been modeled by calculating the thermal conductivity from the fit data for the effective mfp acquired in (a). (c) Effective phonon mfp, calculated from the measured thermal conductivity, as a function of temperature. A combination of Umklapp scattering, point defect scattering, and boundary scattering has been applied to model the data. The value of $\frac{3}{7}d$ for the boundary scattering models the low-temperature data well. (d) Thermal conductivity as a function of the temperature. The data have been modeled by calculating the thermal conductivity from the fit data for the effective mfp acquired in (c). (e) Effective phonon mfp, calculated from the measured thermal conductivity, as a function of temperature. A combination of Umklapp scattering and boundary scattering has been applied to model the data. A reduced value for the maximum of mfp (60 µm $< d$) was observed, giving rise to the assumption of defects in the substrate limiting the mfp. Due to this reduction, intrinsic scattering is present in this sample. Nevertheless, the heat transport through the epitaxial layer proves to be ballistically for $T<$ 70 K. (f) Thermal conductivity as a function of the temperature. The data have been modeled by calculating the thermal conductivity from the fit data for the effective mfp acquired in (e).

to Eq. (1) is used to describe the low-temperature limit in the formalism of Eq. (2). This is discussed in detail below. All curves fitted with the Callaway model are in good agreement with the measured data.

For temperatures >80 K, Umklapp scattering dominates the phonon transport, as shown in Fig. 4. Contrary to the thermal conductivities, there is no anisotropy of the mfp, as expected. An Umklapp scattering fit was applied to the high-temperature data, modeling the points well >80 K. This means no systematic influence of defects is observed here, and the obtained mfps have the quality of material parameters. The phonon mfp for that regime can be expressed by

$$\Lambda = \mathrm{A} \cdot \left[\exp\left(\frac{\Theta_D}{2T} \right) - 1 \right], \tag{8}$$

with the parameter A representing the value of $\Lambda(\Theta_D/2)$, with $A \approx (0.8 \pm 0.1)$nm. A least-square fit of the Umklapp scattering gives a Debye temperature of $\Theta_D = (975 \pm 50)$ K. Previously, a value of $\Theta_D = 870$ K was predicted [39].

Below 80 K, point-defect scattering dominates the transport. Previously, we showed that point defects already play a role at 150 K [15], which indicates higher purity of the material investigated in this paper. In the regime of point-defect scattering, the anisotropy of the thermal conductivity vanishes, as expected. The fit for the point-defect scattering is calculated as

$$\Lambda_{PD} = \Lambda(T_0) \left(\frac{T_0}{T} \right)^4. \tag{9}$$

The measurement data show good agreement with the T^{-4}-Rayleigh model between 30 and 80 K. This fit can be compared with the relation $\Lambda_{PD} = \frac{1}{\Phi n}$ [24], with n as density of point defects and Φ as scattering cross-section. For low temperatures, the scattering cross-section can be expressed as $\Phi = \frac{16\pi^5 R^6}{l_{\mathrm{dom},0}^4 T_0^4} T^4$ [24], with R as atom radius of the scattering centers and $l_{\mathrm{dom},0}$ as dominant phonon wavelength (see Fig. S3 in the Supplemental Material [32]) at temperature T_0. With these relations, the density of scattering centers in the material can be approximated as

$$n = \frac{l_{\mathrm{dom},0}^4}{16\pi^5 R^6 \Lambda(T_0)}, \tag{10}$$

using the fit parameter $\Lambda(T_0)$ with the value of $\Lambda(50\ \mathrm{K}) \approx 6.4\ \mu$m. In a comparison between the known atomic radii [40] and the expected concentrations of each potential atom, the most likely candidates acting as a scattering center are the ^{18}O isotopes within the β-Ga_2O_3 crystal (see Fig. S6 in the Supplemental Material [32]).

The resistive (intrinsic) scattering regime >30 K can be well described by the combination of Umklapp scattering and point-defect scattering in the Callaway model [25].

In detail, we discuss the low-temperature observations below. At low $T < 30$ K, the effective phonon mfp approximates to a constant value. The fits in the low-temperature regime are in good agreement with the data, as shown in Fig. 5.

To describe the low-temperature limit in the formalism of the Callaway model [25], Λ_B is substituted by $\frac{3}{7}\ d$ [17] [see Eq. (2)]. The experimental data are well described by this fixed Λ_{eff} at low temperatures, as can be seen in Fig. 5. This requires an intrinsic phonon mfp in the samples $\Lambda > \approx d$ comparable with the film thickness. The occurrence of both the phonon mfp reaching a plateau at a value of $\frac{3}{7}d$ and the T^3 dependence of the thermal conductivity in this temperature range indicates that the transition from resistive to ballistic phonon transport is observed. Therefore, diffusive interactions with the backside surface of the crystal take place, leading to phonon-radiative heat transport across the crystal. In such a case, resistive scattering processes are negligible, and the interaction with the crystal surfaces dominates the thermal transport properties. However, a phonon mfp of $\frac{3}{4}d$, which would correspond to the case of $\Lambda \gg d$ in the Casimir limit, is not quite achieved, as can be seen in Fig. 5. Nevertheless, it approaches up to 60% at 10 K ($\Lambda > \approx d$).

For the SCB + 2 μm HE sample, the effective phonon mfp approximates to 60 μm, which is much less than the crystal thickness. This can be explained by the existence of defects in the crystal which limit the phonon mfp.

Using the modeled phonon mfps, the thermal conductivity data can be fitted by the relation $\lambda = \frac{1}{3}\Lambda c_P \rho v_S$. This has been performed for all samples, as shown in Figs. 5(b), 5(d), and 5(f). The fits represent the measured thermal conductivity data well for the entire temperature range.

In the context of ballistic phonon transport, the interaction between phonons and the crystal surface is of high importance. Therefore, the surface properties are discussed here. The backsides of all samples (SCB substrates) were not polished, leading to a surface roughness of several microns as determined by atomic force microscopy. To avoid the occurrence of specular reflection at the backside in the case of ballistic phonon transport, the dominant phonon wavelength l_{dom} must be smaller or comparable with the roughness r to ensure diffuse emission. The dominant phonon wavelength can be calculated by a modified version of Wiens law to be $l_{\mathrm{dom}} = hv_s/(2.82\ k_B T)$ with the sound velocity v_s ($v_s = 4318$ m/s in the [100] direction) and temperature T. For $T = 20$ K, this gives a value of $l_{\mathrm{dom}} \approx 4$ nm. This is illustrated in Fig. S3 in the Supplemental Material [32]. Since clearly $l_{\mathrm{dom}} \ll r$, the interaction of phonons with the backside surface of all samples is expected to be diffusive. The top surface of the SCB and the epitaxial layers has a considerably lower roughness (see Fig. 1). In this case, $l_{\mathrm{dom}} \approx r$. Furthermore, as required, it is ensured that the temperature on the top surface of all samples is the higher temperature, as it is in direct thermal contact with the heater line. According to Majumdar [24], the electron-phonon mfp in the metal is much smaller than the phonon mfp in the film, and thus, the interface of the dielectric film can be assumed to be a thermalizing black boundary.

As required, the crystal backside is in thermal contact with the bath temperature. Here, a different situation is prevalent: Due to the roughness $r <\approx 5$ μm of the sample backside, the diffusive mismatch model can be applied [23]. The density of states $N \propto \frac{\omega^2}{v^3}$ (see Fig. S3 in the Supplemental Material [32]) for phonons of a frequency ω is much higher in the glue below the sample due to its considerably lower sound velocity. Therefore, practically all phonons are absorbed into the glue, and their energy dissipates into the thermal bath. The interface can therefore be assumed to be a thermalizing black

boundary fixed at the bath temperature. Thermalized phonons will then be re-emitted diffusively from the rough surface, and a radiative equilibrium will be established.

For the SCB and SCB + 3 μm HE samples, all conditions of the Casimir model [22] have been proven true for temperatures <20 K. The thermal conductivity shows T^3 dependence, while the temperature gradient remains small compared with the bath temperature. The surface roughness of the crystal backside is much higher than the phonon wavelength leading to diffusive interaction between the phonons and the surface. The maximum of effective mfp fits well to the theoretical value of $\frac{3}{7}d$ expected for the case of $\Lambda > \approx d$. We therefore conclude that the crossover from resistive to ballistic transport is observed. Ballistic phonon transport from the heater to the back surface of the crystal takes place. The heat transport can be described as PRT, which is no longer dominated by intrinsic material properties but by the crystal surfaces.

In the case of the SCB + 2 μm HE sample, a ballistic transport of phonons between the two crystal surfaces was not fully achieved. However, the effective phonon mfp still greatly exceeds the thickness of the HE layer. Consequently, the HE interface between the single-crystalline substrate and the MOVPE-grown HE layer is *phonon transparent*: Heat can be transported through the interface without any noticeable thermal resistance. It indicates a high epitaxial growth quality at the interface of single-crystalline substrate and the HE-grown layer. This is of special interest in the case of electrically conductive layers as used in high-power field-effect transistors, where electron transport will be confined to the doped HE electrically conducting layers, whereas the phonons can propagate out of the layer through the entire substrate underneath. This enables a separation of thermal and electrical transport paths.

The above results show that, for sufficiently low temperatures, heat can be transported ballistically through and out of β-Ga_2O_3 HE layers. Currently, electronic devices are often designed to use β-Ga_2O_3 layer thicknesses on the order of 1 μm. An effective phonon mfp of some microns is reached at temperatures of ∼70 K, for a high-crystalline quality of β-Ga_2O_3 comparable with the samples in this paper. At such operating temperatures, near that of liquid nitrogen (77 K), β-Ga_2O_3 has a much higher overall thermal conductivity [$\lambda = (200 \pm 30)$ W/(mK) at 77 K] than at room temperature. This increase in the thermal conductivity is comparable with that of the commonly used high-power material SiC [41]. Advantageously, the electrical conductivity of β-Ga_2O_3 at 77 K is only slightly reduced compared with room temperature (factor 2–3). In contrast, SiC shows a drop in the electrical conductivity of an entire order of magnitude [42].

Below 20 K, the observation of ballistic phonon transport along a macroscopic dimension of 500 μm demonstrates the high crystalline and epitaxial quality of the β-Ga_2O_3 single crystals and HE layers leading to phonon-transparent interfaces. In summary, our findings show that, in high-quality HE β-Ga_2O_3 layers, heat transport may be engineered. This may be of particular interest for applications of electronic devices at cryogenic temperatures of liquid nitrogen.

V. CONCLUSIONS

The room-temperature anisotropy of the thermal conductivity of high-quality β-Ga_2O_3 single crystals and HE layers vanishes for temperatures <80 K, where the role of Umklapp scattering and therefore the monoclinic crystal structure becomes negligible. Between 80 and 30 K, point-defect scattering, presumably by ^{18}O isotopes, dominates the phonon transport. For temperatures <20 K, boundary effects dominate. The effective phonon mfp has been determined to be on the order of 3 nm at room temperature which, in contrast to the thermal conductivity, was observed to be isotropic. It increases to ∼1 μm at 80 K and is limited <20 K by an effective sample size. Modeling of the Umklapp and point-defect scattering succeeds by use of the Callaway model and the size limitation at low temperatures by the Majumdar model. From that, we conclude that the interface between the substrate and the HE layer is phonon transparent and that we observe the crossover from resistive to ballistic heat transport in the PRT regime.

ACKNOWLEDGMENTS

This paper was performed in the framework of GraFOx II, a Leibniz-ScienceCampus, and was partially funded by the Leibniz association and by the Deutsche Forschungsgemeinschaft (Grants No. 289649665 with parts FI932/10–2, and No. PO 2659/1–2). The authors would like to thank Martin Schmidbauer for fruitful scientific discussions.

[1] H. H. Tippins, Optical absorption and photoconductivity in the band edge of β-Ga_2O_3, Phys. Rev. **140**, A316 (1965).

[2] M. R. Lorenz, J. F. Woods, and R. Gambino, Some electrical properties of the semiconductor β-Ga_2O_3, J. Phys. Chem. Solids **28**, 403 (1967).

[3] M. Orita, H. Ohta, M. Hirano, and H. Hosono, Deep-ultraviolet transparent conductive β-Ga_2O_3 thin films, Appl. Phys. Lett. **77**, 4166 (2000).

[4] S. I. Stepanov, V. I. Nikolaev, V. E. Bourgrov, and A. E. Romanov, Gallium oxide: Properties and applications—A review, Rev. Adv. Mater. Sci. **44**, 63 (2016).

[5] E. Fortunato, D. Ginley, H. Hosono, and D. C. Paine, Transparent conducting oxides for photovoltaics, MRS Bull. **32**, 242 (2007).

[6] A. J. Freeman, K. R. Poeppelmeier, T. O. Mason, R. P. H. Chang, and T. J. Marks, Chemical and thin-film strategies for new transparent conducting oxides, MRS Bull. **25**, 45 (2000).

[7] N. Suzuki, S. Ohira, M. Tanaka, T. Sugawara, K. Nakajima, and T. Shishido, Fabrication and characterization of transparent conductive Sn-doped β-Ga_2O_3 single crystal, Phys. Status Solidi C **4**, 2310 (2007).

[8] S. J. Pearton, J. Yang, P. H. Cary, F. Ren, J. Kim, M. J. Tadjer, and M. A. Mastro, A review of Ga_2O_3 materials, processing, and devices, Appl. Phys. Rev. **5**, 01130 (2018).

[9] Z. Galazka, β-Ga_2O_3 for wide-bandgap electronics and optoelectronics, Semicond. Sci. Technol. **33**, 113001 (2018).

[10] M. Higashiwaki, K. Sasaki, A. Kuramata, T. Masui, and S. Yamakoshi, Development of gallium oxide power devices, Phys. Status Solidi A **211**, 21 (2014).

[11] M. Higashiwaki, A. Kuramata, H. Murakami, and Y. Kumagai, State-of-the art technologies of gallium oxide power devices, J. Phys. D Appl. Phys. **50**, 333002 (2017).

[12] Z. Liu, P. Li, Y. Zhi, X. Wang, X. Chu, and W. Tang, Review of gallium oxide based field-effect transistors and Schottky barrier diodes, Chin. Phys. B **28**, 017105 (2019).

[13] M. L. Levinshtein, S. L. Rumyantsev, and M. S. Shur, *Properties of Advanced Semiconductor Materials GaN, AlN, SiC, BN, SiC, SiGe* (John Wiley & Sons, Inc., New York, 2001).

[14] Z. Guo, Z. Guo, A. Verma, X. Wu, F. Sun, A. Hickman, T. Masui, A. Kuramata, M. Higashiwaki, D. Jena *et al.*, Anisotropic thermal conductivity in single crystal β-gallium oxide, Appl. Phys. Lett. **106**, 111909 (2015).

[15] D. Klimm, B. Amgalan, S. Ganschow, A. Kwasniewski, Z. Galazka, and M. Bickermann, The thermal conductivity tensor of β-Ga_2O_3 from 300 to 1275 K, Cryst. Res. Technol. **58**, 2200204 (2023).

[16] A. J. Green, J. Speck, G. Xing, P. Moens, F. Allerstam, K. Gumaelius, T. Neyer, A. Arias-Purdue, V. Mehrotra, A. Kuramata *et al.*, β-gallium oxide power electronics, APL Mater. **10**, 029201 (2022).

[17] M. Handwerg, R. Mitdank, Z. Galazka, and S. F. Fischer, Temperature-dependent thermal conductivity in Mg-doped and undoped β-Ga_2O_3 bulk-crystals, Semicond. Sci. Technol. **30**, 024006 (2015).

[18] M. Handwerg, R. Mitdank, Z. Galazka, and S. F. Fischer, Temperature-dependent thermal conductivity and diffusivity of a Mg-doped insulating β-Ga_2O_3 single crystal along [100], [010] and [001], Semicond. Sci. Technol. **31**, 125006 (2016).

[19] Y. Song, P. Ranga, Y. Zhang, Z. Feng, H.-L. Huang, M. D. Santia, S. C. Badescu, C. U. Gonzalez-Valle, C. Perez, K. Ferri *et al.*, Thermal conductivity of β-phase Ga_2O_3 and $(Al_xGa_{1-x})_2O_3$ heteroepitaxial thin films, ACS Appl. Mater. Interfaces **13**, 38477 (2021).

[20] Y. Zhang, Q. Su, J. Zhu, S. Koirala, S. J. Koester, and X. Wang, Thickness-dependent thermal conductivity of mechanically exfoliated β-Ga_2O_3 thin films, Appl. Phys. Lett. **116**, 202101 (2020).

[21] Z. Cheng, L. Yates, J. Shi, M. J. Tadjer, K. D. Hobart, and S. Graham, Thermal conductance across β-Ga_2O_3-diamond van der Waals heterogeneous interfaces, APL Mater. **7**, 031118 (2019).

[22] H. Casimir, Note on the conduction of heat in crystals, Physica **5**, 495 (1938).

[23] E. T. Swartz and R. O. Pohl, Thermal boundary resistance, Rev. Mod. Phys. **61**, 605 (1989).

[24] A. Majumdar, Microscale heat conduction in dielectric thin films, J. Heat Transfer **115**, 7 (1993).

[25] J. Callaway, Model for lattice thermal conductivity at low temperatures, Phys. Rev. **113**, 1046 (1959).

[26] Z. Galazka, R. Uecker, K. Irmscher, M. Albrecht, D. Klimm, M. Pietsch, M. Brützam, R. Bertram, S. Ganschow, and R. Fornari, Czochralski growth and characterization of β-Ga_2O_3 single crystals, Cryst. Res. Technol. **45**, 1229 (2010).

[27] Z. Galazka, K. Irmscher, R. Uecker, R. Bertram, M. Pietsch, A. Kwasniewski, M. Naumann, T. Schulz, R. Schewski, D. Klimm *et al.*, On the bulk β-Ga_2O_3 single crystals grown by the Czochralski method, J. Cryst. Growth **404**, 184 (2014).

[28] Z. Galazka, R. Uecker, D. Klimm, K. Irmscher, M. Naumann, M. Pietsch, A. Kwasniewski, R. Bertram, S. Ganschow, and M. Bickermann, Scaling-up of bulk β-Ga_2O_3 single crystals by the Czochralski method, ECS J. Solid State Sci. Technol. **6**, Q3007 (2017).

[29] Z. Galazka, Growth of bulk β-Ga_2O_3 single crystals by the Czochralski method, J. Appl. Phys. **131**, 031103 (2022).

[30] G. Wagner, M. Baldini, D. Gogova, M. Schmidbauer, R. Schewski, M. Albrecht, Z. Galazka, D. Klimm, and R. Fornari, Homoepitaxial growth of β-Ga_2O_3 layers by metal-organic vapor phase epitaxy, Phys. Status Solidi A **211**, 27 (2014).

[31] T.-S. Chou, P. Seyidov, S. Bin Anooz, R. Grüneberg, T. T. V. Tran, K. Irmscher, M. Albrecht, Z. Galazka, J. Schwarzkopf, and A. Popp, Fast homoepitaxial growth of (100) β-Ga_2O_3 thin films via MOVPE, AIP Adv. **11**, 115323 (2021).

[32] See Supplemental Material at http://link.aps.org/supplemental/10.1103/PhysRevB.110.085302 for details of the (S1) resistivity of the metal heater line, (S2) the room temperature thermal conductivity, (S3) phonon spectral density, (S4) TEM images, (S5) further thermal conductivity data, (S6) density of point defects, and (S7) thermal penetration depth.

[33] D. G. Cahill, Thermal conductivity measurement from 30 to 750 K: The 3ω method, Rev. Sci. Instrum. **61**, 802 (1990).

[34] D. G. Cahill, H. E. Fischer, T. Klitsner, E. T. Swartz, and R. O. Pohl, Thermal conductivity of thin films: Measurements and understanding, J. Vac. Sci. Technol. A **7**, 1259 (1989).

[35] H. S. Carslaw and J. C. Jaeger, *Conduction of Heat in Solids* (Oxford University Press, Oxford, 1959).

[36] F. Völklein, H. Reith, T. W. Cornelius, M. Rauber, and R. Neumann, The experimental investigation of thermal conductivity and the Wiedemann-Franz law for single metallic nanowires, Nanotechnology **20**, 325706 (2009).

[37] M. D. Santia, N. Tandon, and J. D. Albrecht, Lattice thermal conductivity in β-Ga_2O_3 from first principles, Appl. Phys. Lett. **107**, 041907 (2015).

[38] T.-S. Chou, P. Seyidov, S. Bin Anooz, R. Grüneberg, J. Rehm, T. T. V. Tran, A. Fiedler, K. Tetzner, Z. Galazka, M. Albrecht *et al.*, High-mobility 4 μm MOVPE-grown (100) β-Ga_2O_3 film by parasitic particles suppression, Jpn. J. Appl. Phys. **62**, SF1004 (2023).

[39] H. He, M. A. Blanco, and R. Pandey, Electronic and thermodynamic properties of β-Ga_2O_3, Appl. Phys. Lett. **88**, 261904 (2006).

[40] R. D. T. Shannon and C. T. Prewitt, Effective ionic radii on oxides and fluorides, Acta Cryst. B **25**, 925 (1969).

[41] G. A. Slack, Thermal conductivity of pure and impure silicon, silicon carbide, and diamond, J. Appl. Phys. **35**, 3460 (1964).

[42] E. A. Burgemeister, W. von Muench, and E. Pettenpaul, Thermal conductivity and electrical properties of 6H silicon carbide, J. Appl. Phys. **50**, 5790 (1979).